Using polarization to estimate surface normals at air–water interfaces for correction of refraction in seafloor imaging

Enno Peters,[1],* **Gary A. Atkinson,[2] and Maurice Stephan[1]**

[1]*Institute for the Protection of Maritime Infrastructures, German Aerospace Center (DLR), Fischkai 1, 27572 Bremerhaven, Germany*
[2]*Centre for Machine Vision, Bristol Robotics Laboratory, University of the West of England Bristol, BS16 1QY, UK*
Enno.Peters@dlr.de

The retrieval of sea surface normal vectors using shape-from-polarization is investigated for the purpose of correcting for refraction at the water–air interface when imaging from above the water. In shallow clear water and overcast conditions, spectral longpass filtering (using a hard-coated 850 nm cut-on wavelength filter) is demonstrated to 1) avoid artifacts from the ground in the measured polarization state, and 2) reduce polarization from water-leaving radiance sufficiently to derive shape information exclusively from the polarization produced by specular reflection. The dependence of the method on meteorological conditions is studied. Measurements are performed with a commercial polarization filter array (PFA) camera. Due to the decreasing PFA efficiency towards the near-infrared, rigorous characterization and calibration measurements were performed and recommendations (e.g., on the f-number) elaborated. Overcoming the paraxial approximation, normal vectors are then retrieved with systematic errors of 0.1° (image center) to 0.5° − 0.8° (edges/corners) for a flat water surface. An image of the sea floor corrected for surface refraction shows maximum displacements of 10–20 pixels only (corresponding to 0.25°) with respect to a validation image without water.

1. INTRODUCTION

When light from a submerged object passes the sea–air interface, it is refracted according to Snell's law so that the object appears under a wrong angle when observed from above (e.g., by an aerial camera). If the water surface is non-planar (e.g., waves), the problem is even worse as additional image distortions are introduced, for which different methods ranging from pure software algorithms to hardware solutions have been proposed [1–4]. More recently, the so-called fluid lensing technology was developed exploiting time-varying optical lensing effects caused by surface waves, and successfully used from drones [5,6]. Other studies have shown that polarization can be exploited to increase or decrease the measured ratio of light reflected at the surface to light arising from the water body. This has been successfully used for enhancing the visibility through the water surface [7]. However, direct image correction is possible if the spatial distribution of surface slopes is available [8]. In the present study, we use passive polarization imaging under skylight to recover the orientation of water surface normals and use the results to correct for refraction in the image of the sea floor.

A. Related Work

The polarization nature of light is used in many applications ranging from vision enhancement above the water [9,10] as well as underwater [11,12] to industrial purposes like visualization of stress [13] and shape analysis in computer vision [14,15]. In such cases, the so-called shape-from-polarization technique is often based on diffuse reflection caused by multiple subsurface scattering [16,17], while specular reflection is avoided by the experimental setup. In this optimal case, the polarization state of the illumination is destroyed by the reflection process and the observed polarization is exclusively caused by refraction at the material–air interface. By contrast, specular reflection of skylight is omnipresent in daytime outdoor measurements, so the observed polarization from the water surface is a superposition of: 1) the polarization of the incoming light, 2) polarization caused by specular reflection at the sea surface, and 3) underwater effects including polarization due to refraction of subsurface scattered light when re-entering into the air.

The theory of polarization effects in water and at the surface is well known [18,19], and the recovery of sea surface slopes from polarization data was demonstrated by several former studies using different instrument designs and deployments

ranging from ground-based to ship- and air-borne platforms [20–26]. Measurements were mostly performed in cases of unpolarized skylight, i.e., overcast conditions [20,21], using a Rayleigh model to approximate the polarization of the blue skylight [22,24], or incorporated measurements of the skylight polarization [25,26]. Some studies addressed the ambiguity of the degree of linear polarization (DoLP) produced by specular reflection, which does not have a 1-to-1 relationship with surface angle [24,27]. Also, the need for fast measurements to avoid motion blur is emphasized [21]. An under-investigated problem in older studies is the polarization caused by upwelling light, which was sometimes argued to be negligible [21], explicitly mentioned as an error source but not incorporated in the data retrieval [22] or treated as a bias when having multiple frames [20]. However, some studies indicated that including a contribution of upwelling radiance improves the results [24]. In the domain of remote sensing, the polarization of light fields reflected from the water surface [28,29] as well as transfer functions of the ocean surface [30] were investigated in more detail, and the retrieval of water optical parameters was reported using hyperspectral polarimetric imaging [31]. Recently, Malinowski *et al*. reported about ocean wave slope statistics obtained with an improved and modified Polarimetric Slope Sensing technique [25,26] which was used at different wavelength bands in the Visible and eliminated the contribution of polarization from upwelling radiance. A summary of challenges and fundamental principles of shape-from-polarization techniques can be found, e.g., in [32].

B. Contributions

This study is a proof of concept and accuracy estimation for the proposed method. A polarization filter array (PFA) camera is used measuring the Degree and Angle of linear polarization (DoLP, resp. AoLP) simultaneously. As the addressed scenario is seafloor imaging in clear, shallow waters, the PFA camera is equipped with spectral longpass filters to avoid artifacts from the ground in the DoLP and AoLP. At the same time, the longpass filters increase the ratio of specular reflected to water-leaving radiance, enabling the retrieval of surface normals from polarization caused by specular reflection alone. Different spectral filters and the effect of different weather conditions for this method are investigated.

A final instrument (which is out of scope of the current study) could then consist of two channels, a polarization-sensitive camera and a visual camera with inherent pixel matching, e.g., sharing the same optics. The polarization-sensitive channel is suggested to be equipped with a spectral longpass filter, and derives surface normals which are used to correct sea floor images of the visual camera. The current study demonstrates the general feasibility of this idea and provides a case example, investigates achievable accuracies and limitations with state-of-the-art technology, and investigates the influence of meteorological conditions.

The manuscript is structured as follows: The relevant theory and technology used is described in Section 2. As the extinction ratio of the PFA camera strongly decreases with wavelength, extensive calibration efforts are carried out in Section 3. In

Section 4, the proposed suppression of polarization from water-leaving radiance, and artifacts from the seafloor are investigated under different meteorological conditions. Focusing on clear water, surface normals are then retrieved and the corresponding uncertainty is estimated (Section 5). An added value of the retrieval is that it overcomes the paraxial approximation, i.e., projection of the lens is explicitly taken into account, which is a further methodological limitation of many previous studies [33]. A detailed mathematical derivation of the retrieval and used equations are therefore provided as a supplement. In Section 6, using the surface normals as an input, refraction at the water surface is corrected for in an image of the seafloor (bottom of a clear water tank).

2. METHODOLOGY

A. Measurement Technique and Instrumentation

The camera used in this study is a division-of-focal-plane polarimeter model DZK 33UX250 from The Imaging Source using a monochromatic CMOS Pregius Polarsens sensor (Sony IMX250MZR) having 2448×2048 used pixels. The camera sensor is equipped with a polarization filter array (PFA) consisting of 2×2 sets of micropolarizers measuring the irradiance I_0, I_{45}, I_{90}, and I_{135} polarized in the 0°, 45°, 90° and 135° directions simultaneously (counterclockwise with 0° being the horizontal direction). For sensor operation, C++ in-house software was developed based on the vendor SDK reading the 12-bit camera raw data.

Different methods exist to convert the PFA camera's raw data to Stokes vectors [15,34,35]. The original and most basic method (as used here) considers each 2×2 set of pixels as a superpixel, resulting in 1224×1024 superpixels in total. The Stokes vector for each superpixel is

$$\boldsymbol{S} = \begin{pmatrix} S_0 \\ S_1 \\ S_2 \\ S_3 \end{pmatrix} = \begin{pmatrix} \frac{I_0 + I_{45} + I_{90} + I_{135}}{2} \\ I_0 - I_{90} \\ I_{45} - I_{135} \\ I_R - I_L \end{pmatrix}, \tag{1}$$

where S_0 is the total irradiance, S_1 is the excess of 0° polarization over 90°, S_2 the excess of 45° over 135°, and S_3 the excess of right-handed over left-handed polarization. Note that circular polarization is not measurable with the camera used. However, sources of circular polarization are rare in nature, and in particular, surface reflection above the water produces only linear polarization (e.g., [15,22] and references therein). Thus, for the specific application, S_3 can be neglected.

For each superpixel, the degree of linear polarization (DoLP) and the angle of linear polarization (AoLP) are obtained from the Stokes vector's elements by [36]:

$$\text{DoLP} = \frac{\sqrt{S_1^2 + S_2^2}}{S_0}, \tag{2}$$

$$\text{AoLP} = \frac{1}{2} \arctan_2\left(\frac{S_2}{S_1}\right), \tag{3}$$

where $\arctan_2$ is the four-quadrant inverse tangent [37]. The AoLP is the angle in which the radiation's electric field has on

average its largest component, i.e., if DoLP = 1, then all light is polarized in this direction.

For this study, the PFA camera was equipped with a model LM25HC 25 mm fixed focal length lens from KOWA, enabling f-numbers from f/1.4 to f/16. With the camera's pixel width of 3.45 μm × 3.45 μm, the field of view (FOV) of an individual pixel is $\text{FOV}_{\text{pix}} \approx 0.008°$, and $\text{FOV}_{\text{super}} \approx 0.016°$ for a superpixel. At a working distance of 2 m, this corresponds to a resolution of ~0.6 mm per superpixel. This is sufficient to consider the surface observed by a single superpixel to be flat, which is crucial as any unresolved curvature would bias the measurement, e.g., the measured DoLP could not reach 1 at Brewster's angle. The total FOV of the instrument is $\text{FOV}_{\text{v}} \approx 16.1°$ vertically and $\text{FOV}_{\text{h}} \approx 19.3°$ horizontally.

The camera–lens combination could be equipped with different spectral longpass filters, which are described in detail in Section 3.A.

B. Fresnel Coefficients, Expected DoLP, and AoLP

Reflection at and transmission (i.e., refraction) through the water–air interface are described by Fresnel coefficients [36]. The intensity reflection coefficients (reflectances) R_s and R_p for light components polarized perpendicular and parallel to the plane of incidence are:

$$R_s = \left| \frac{n_i \cos \theta_i - n_t \cos \theta_t}{n_i \cos \theta_i + n_t \cos \theta_t} \right|^2, \qquad (4)$$

$$R_p = \left| \frac{n_t \cos \theta_i - n_i \cos \theta_t}{n_t \cos \theta_i + n_i \cos \theta_t} \right|^2. \qquad (5)$$

Here, n_i and n_t are the refractive indices of the incidence and reflecting (resp. entered) media, θ_i is the incidence angle, θ_r the reflected angle, and θ_t the refracted angle, which is calculated using Snell's law. The corresponding intensity transmission coefficients (transmittances) are $T_p = 1 - R_p$ and $T_s = 1 - R_s$. The scattering geometry for specular reflection in a certain angle $\theta_r = \theta_i$ (hereafter called *specular reflected ray*) and of upwelling refracted radiance in direction θ_t (hereafter called *water-leaving ray*) is shown in Figs. 1(a) and 1(b). Note that the change of direction of the water-leaving ray is the reason for image distortions of underwater scenes.
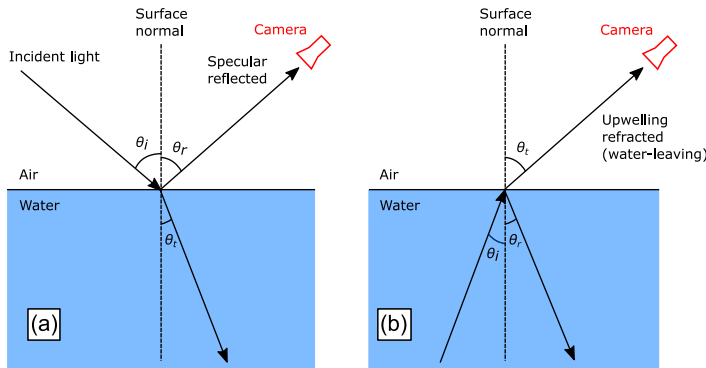
For specular reflection, the DoLP is obtained from reflectances in Eqs. (4) and (5) using $n_i = 1$ (air) and $n_t = 1.33$ (water):

$$\text{DoLP}_{\text{spec}} = \frac{R_s - R_p}{R_s + R_p}. \qquad (6)$$

The DoLP of the water-leaving ray is obtained from transmittances T_s and T_p, but using $n_i = 1.33$ (water) and $n_t = 1$ (air) and limiting the incidence angle to Snell's window:

$$\text{DoLP}_{\text{water}} = \frac{T_p - T_s}{T_s + T_p}. \qquad (7)$$

In Fig. 1(c), the reflectances, transmittances, and the resulting DoLPs are plotted as a function of camera view angle $\theta = \theta_r = \theta_i$ for specular reflection and $\theta = \theta_t$ for water-leaving rays. For specular reflection, $R_s > R_p$ for all angles θ, i.e., the direction of the produced polarization ($\text{AoLP}_{\text{water}}$) is always perpendicular to the plane of incidence. The resulting $\text{DoLP}_{\text{spec}}$ peaks at the Brewster angle (complete polarization), which is $\theta_B \approx 53°$ for an air–water interface. Since the $\text{DoLP}_{\text{spec}}$ reduces at either side of θ_B, there exists an ambiguity, i.e., a 2-to-1 relationship between $\text{DoLP}_{\text{spec}}$ and θ, making the retrieval of θ from a measurement of the $\text{DoLP}_{\text{spec}}$ an ill-posed problem. This was addressed in several previous studies [24,27], but is not on focus of this study. To retrieve θ in the following sections, we use *a priori* knowledge about which side of the maximum applies to any given pixel.

For upwelling light refracted at the surface (water-leaving ray), the parallel component is larger than the perpendicular component ($T_p > T_s$) for all angles θ. Consequently, the produced $\text{AoLP}_{\text{water}}$ is parallel to the plane of incidence. $\text{DoLP}_{\text{water}}$ is monotonously increasing until $\theta = 90°$, i.e., it has no ambiguity.

As mentioned, the radiance reaching the camera is a superposition of specular reflected skylight (perpendicular polarization) and water-leaving radiance (parallel polarization), and the relative contributions strongly depend on viewing geometry, optical properties of the water (scatterers), and weather conditions, which is investigated in Section 4.
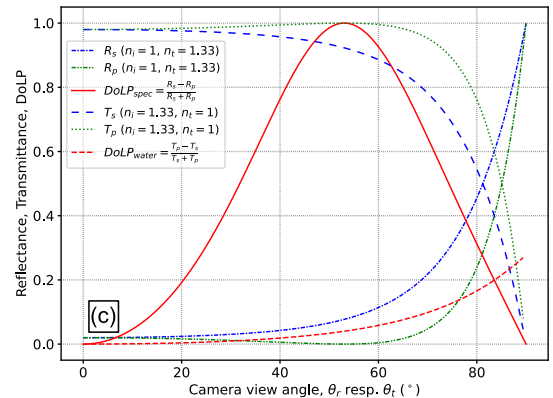
Fig. 1. Scattering geometry for (a) specular reflection of skylight and (b) refraction of upwelling radiation when leaving the water. (c) Corresponding Fresnel reflectances, transmittances, and resulting DoLPs as a function of view angle.

C. Retrieval of Surface Normals Including Paraxial Correction

The proposed surface normal retrieval is applied to each superpixel and has inputs of:

• θ, the angle between water surface normal and viewing vector. It is obtained by inverting the measured DoLP assuming that water-leaving contributions are sufficiently reduced, i.e., measured $\text{DoLP} = \text{DoLP}_{\text{spec}}$ (which is a function of θ as shown in Fig. 1(c)). The measured DoLP is obtained for each superpixel from measured intensities I_0, I_{45}, I_{90}, I_{135} using Eqs. (1) and (2).

• Φ, the angle of the surface normal projected into the imaging plane. It is directly obtained from the measured AoLP (the angle of linear polarization projected into the imaging plane), which is calculated from measured intensities I_0, I_{45}, I_{90}, I_{135} using Eqs. 1 and 3 (see Supplement 1 for detailed definitions).

• α and β, the horizontal and vertical viewing angles of the respective superpixel with respect to the optical axis.

• ϑ, the (measured) pitch angle of the camera's optical axis pointing down to the water surface. The camera's roll and yaw angles were adjusted to 0° in experiments throughout this study.

As the derivation of the proposed surface normal retrieval is lengthy, it is provided in detail in Supplement 1. In summary, first, surface normals $\mathbf{n}$ are retrieved from the above-mentioned inputs in the camera coordinate system. In this step, the perspective projection of the lens is compensated for. In the second step, the camera coordinate system is then rotated by the pitch angle ϑ to obtain $\mathbf{n} = (n_x, n_y, n_z)$ in an orthogonal $\mathbf{xyz}$ coordinate system, which is indicated in Fig. 2 showing an experimental setup with PFA camera above a planar water surface (this experiment and retrieved surface normals are presented in Section 5). The $\mathbf{x}$-axis is on the water surface from left to right, $\mathbf{y}$ is perpendicular to the water surface (i.e., zenith-pointing) and $\mathbf{z}$ is again on the water surface pointing from horizon to camera, forming a right-handed coordinate system with the $\mathbf{xz}$-plane being the water surface.

It is worth noting that in most previous studies using shape-from-polarization techniques, the camera coordinate system
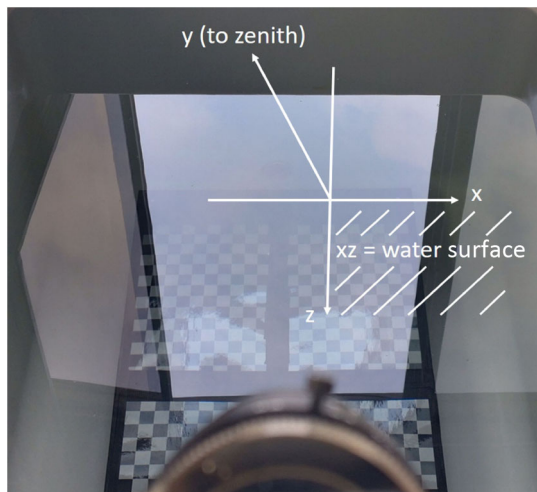
was merely rotated by the camera (pitch) angle for conversion to a convenient outer world coordinate system, corresponding to the second step of our retrieval. However, this is valid only for center pixels as the viewing vector is then on the optical axis and orthogonal to the imaging plane. If the focal length of the system is large, the resulting error for pixels off the optical axis is small (paraxial approximation). However, the FOV here is 16.1° × 19.3°, and therefore the angle between viewing vector and optical axis is as large as ~12.5° in the image corners, requiring a paraxial correction.

To quantify uncertainties of the retrieved surface normals (Section 5), and as input for correcting refraction in images of the sea floor taken from above the water (Section 6), angles w_{yx} and w_{yz} are used describing the pitch of the surface normals from the vertical ($\mathbf{y}$-axis) towards the $\mathbf{x}$-axis and $\mathbf{z}$-axis:

$$w_{yx} = \tan(n_x/n_y), \qquad w_{yz} = \tan(n_z/n_y). \qquad \textbf{(8)}$$

3. CHARACTERIZATION AND CALIBRATION OF THE OPTICAL SYSTEM

A. Spectral Longpass Filters

Two different 850 nm longpass filters could be installed within the PFA camera (see below): a hard-coated filter (Thorlabs Part FELH0850) and a colored glass filter (Thorlabs Part FGL850). The transmission spectra of both filters were measured using a stabilized tungsten-halogen light source (Thorlabs Part SLS201L/M) and a fiber optic spectrometer (Avantes AvaSpec-3648), and are plotted in Fig. 3 together with the liquid water absorption coefficient from the literature [38]. As the water absorption increases with wavelength, the incoming skylight transmitted into the water and then backscattered to the instrument is largely damped by water in the near-infrared (NIR), i.e., in the transmission range of the filters. In the Visible, much more light from underwater backscattering (or reflection at the sea floor) reaches the instrument, but this light is blocked by the filters. Consequently, the contribution of water-leaving radiance is reduced when observing the water surface with filters installed.

The hard-coated filter is based on dielectric coatings and uses interference effects to reject wavelengths below 850 nm. As polarization aberrations are caused by the effect of Fresnel

Fig. 2. Experimental setup to recover surface normals in the coordinate system $\mathbf{xyz}$. The $\mathbf{y}$-axis is zenith-pointing, and $\mathbf{xz}$ is the water surface (see text).
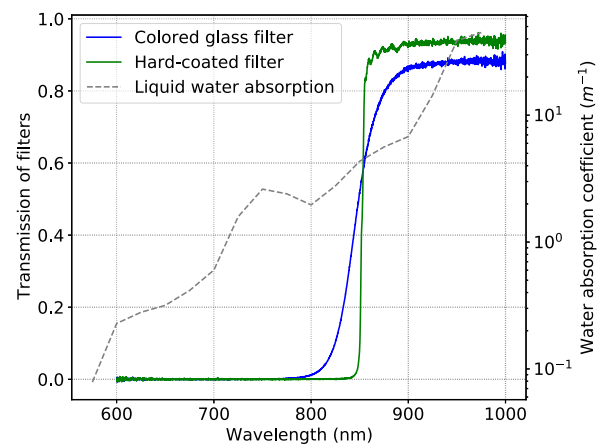
Fig. 3. Transmission spectra of the two investigated longpass filters and absorption coefficient of liquid water (in logarithmic scale).

equations and thin film equations [36], it is expected to bias the measured polarization more than the colored glass filter, which works by absorption. However, the hard-coated filter provides better throughput in the transmission range, a larger optical depth in the blocking range, and a steeper edge at the cut-on wavelength.

B. Polarimetric Calibration

The PFA's efficiency is optimized for the visible spectral range and decreases towards longer wavelengths. Use of spectral longpass filters therefore results in larger amounts of wrong polarization leaking through the PFA. The complete camera-lens system was thus characterized and calibrated for each f-number (f/16, f/8, f/4, f/2.8, f/2, and f/1.4) in three different configurations: 1) without filter, 2) with colored glass filter, and 3) with hard-coated filter.

The experimental setup is shown in Fig. 4(a). The instrument consisting of PFA camera, lens, and optional spectral filter is placed immediately behind an external linear polarizer (Edmund Optics Inc #18943) installed on a rotation mount (Thorlabs Part RSP2/M). The polarizer has a broad spectral efficiency exceeding the quantum efficiency of the camera. For each configuration and f-number, measurement sequences were performed with the polarizer rotated in 10° steps between $\phi = 0°$ and $\phi = 180°$. To reduce temporal noise, ten individual measurements were averaged for each polarizer angle ϕ.

Spectral longpass filters could be installed between the lens and the camera's protective glass window covering pixels, PFA and microlenses [Fig. 4(a)], enabling a compact and robust setup. However, inclusion inside the focusing optics means larger angles of light rays impinging the filters and, as a result of Fresnel equations, altering the measured polarization, which is a further reason for the calibration efforts presented here.

As a light source, unpolarized skylight under overcast conditions was used (it was checked prior to the measurements that the skylight was unpolarized by pointing the PFA camera without longpass filter towards the sky). The calibration requires a flatfield illumination to avoid artifacts arising from intensity gradients within individual superpixels. To achieve flatfield illumination, the camera was either focused on a white Polyoxymethylene (POM) sheet installed in transmission in an open laboratory window diffusing the incoming daylight, or it was directly pointed towards the white cloud layer in cases of

very homogeneous and stable overcast conditions (when having a single and homogeneous cloud layer only). The advantage of using the POM sheet is a more stable flatfield illumination; it was therefore used for the extensive and time-consuming measurement sequences in this section to characterize and compare the instrument with different spectral filters and f-numbers, and to elaborate the improvement after calibration. However, although POM appears white in the visible range, absorption bands exist at wavelengths >850 nm and therefore the transmitted light in the infrared has a slightly different spectrum than skylight. Example measurements with longpass filters revealed DoLP differences of 1%–2% between using POM and clouds, with the latter being preferred as resembling the later used spectrum in outdoor applications. The instrument was therefore calibrated again using clouds. However, this required very homogeneous cloud conditions and was performed only for specific camera settings (filter, f-number) used in later Sections 4–6.

Figure 4(b) shows example results of the measured DoLP in the image center (average of central 100×100 pixels) as a function of polarizer angle ϕ. The DoLP decreases for small f-numbers, which can be again explained by Fresnel equations and increasing angles between light rays and glass interfaces of the optics, making the lens itself a source of polarization [36]. In addition, the DoLP shows variations as a function of ϕ, indicating polarization-dependent throughput of the camera–lens combination. When including longpass filters, the DoLP is further decreased, as expected, because of the smaller PFA's efficiency towards the infrared.

In Fig. 5(a), the uncalibrated DoLP as shown in Fig. 4(b) was averaged over all polarizer angles ϕ and plotted as a function of f-number. Error bars are the corresponding standard deviations representing the variability of the DoLP with ϕ. For all configurations (no filter, colored glass, hard-coated), the average DoLP reaches a plateau for f-numbers > f/4, and decreases for smaller f-numbers. This behavior was found in previous studies [39] as well, where it was attributed to reduced polarization efficiency of the PFA and possibly focusing problems of the on-chip micro-lenses in front of the PFA at large angles of incidence, as a pixel receives light from a cone subtended by the aperture of half-angle $\vartheta = \arctan(1/(2 \times f - \text{number}))$. Interestingly, for the used camera-lens-system, f/4 is the f-number where this cone exceeds the FOV of the camera, i.e., at f-numbers > f/4, largest angles of incidence (inside the optics) reaching
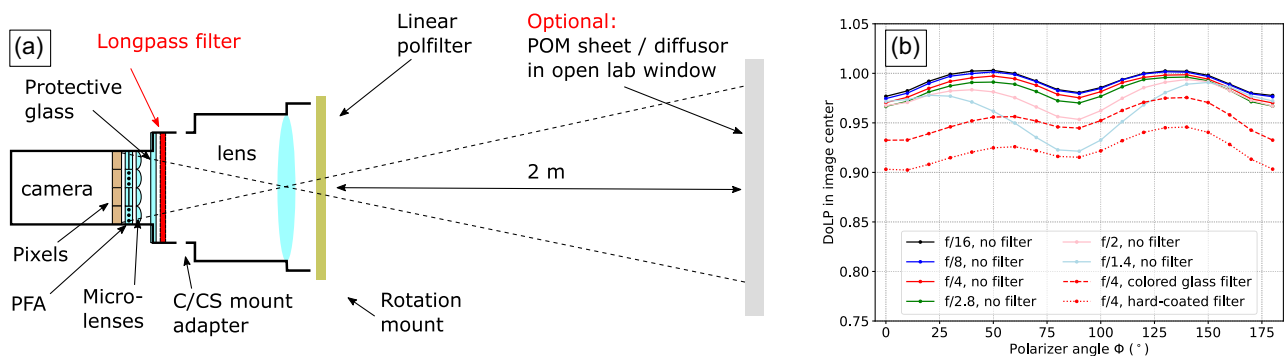
Fig. 4. (a) Experimental setup of the polarization characterization and calibration measurements. (b) Examples of the measured DoLP in the image center as a function of polarizer angle ϕ.
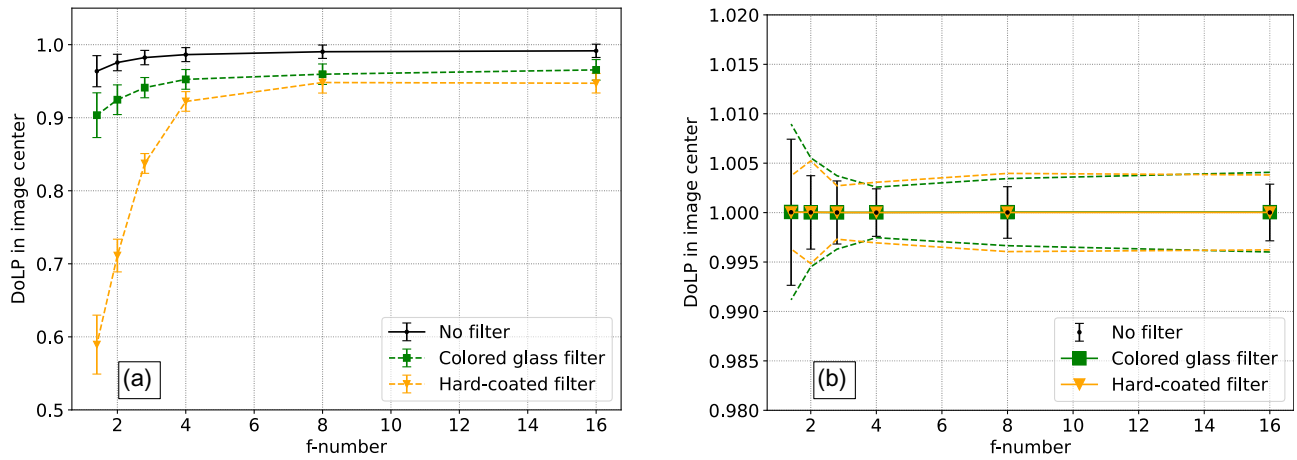
Fig. 5. (a) DoLP (in the image center) averaged over all polarization angles and plotted as function of the f-number. Error bars are standard deviations. (b) Same lines after calibration. For better visualization, errors are plotted as bars for the configuration without filter only, and are indicated by dashed lines for the other configurations. Note the different y-axis scale between (a) and (b).

a pixel are determined by the camera FOV (resulting in the observed plateau), while for f-numbers $<$ f/4, angles of incidence are further increased by the camera aperture. To conclude a best practices recommendation, the f-number of the system should be matched to the FOV (here f/4), avoiding internal reflections or scattering in the optic system to contribute to the measurement.

As seen before, inclusion of longpass filters reduces the DoLP, the hard-coated filter having an even larger effect than the colored-glass filter as expected from their working principles (Section 3.A). However, the hard-coated filter exhibits a very strong decrease for f-numbers $<$f/4 indicating that it is much more vulnerable to the above-mentioned phenomena.

The performed calibration procedure follows an established method for division-of-focal-plane polarimeters [39,40]. As an input, the calibration uses normalized Stokes vector elements, 1) calculated from measurements with rotated polarizer [as shown in Fig. 4(b)], and 2) corresponding theoretical (expected) values from known polarizer angle. A calibration matrix G is then obtained for every superpixel. A detailed explanation is provided in Supplement 1 together with a case example.

Figure 5(b) shows the same as Fig. 5(a), but after calibration. Most prominent is that systematic differences have disappeared and, on average, DoLP $=$ 1 is achieved for each configuration and f-number. Error bars are again standard deviations, which are reduced to $<$1% and even $<$0.5% when considering only f-numbers $> =$ f/4. However, the calibration is applied here

to the same measurements it is obtained from. In practice, the calibration will be applied to new measurements acquired under potentially different conditions. Taking into account the strong degradation of almost 50% using the hard-coated filter at small f-numbers, it is recommended to be used only for f/4 or larger. Consequently, in the following sections we always applied f/4.

Table 1 summarizes for each configuration the errors obtained for f/4 before and after the calibration. Uncalibrated DoLP errors are systematic differences to DoLP $=$ 1 as shown in Fig. 5(a), whereas calibrated DoLP errors are the standard deviations from Fig. 5(b).

AoLP errors were obtained similarly from the same measurements, but the applied polarizer angle ϕ has been subtracted from each measured AoLP, giving the difference to the true polarization angle. Then again, the average and its standard deviation over all polarizer angles ϕ were calculated for each f-number and configuration. In contrast to the DoLP, systematic differences between the uncalibrated and true AoLP were found to be small and well below standard deviations, which were consequently regarded as AoLP errors and included in Table 1.

The AoLP error is in units of degree and thus, if neglecting projection, translates directly into the error of the retrieved surface normals. In contrast, the DoLP error has different impacts. Close to the Brewster angle or in nadir geometry (down facing when assuming a flat surface), the slope of the DoLP as function of θ is small (see Fig. 1), and thus small errors of the DoLP

Table 1. DoLP and AoLP Errors Obtained for f/4 in the Image Center and Averaged Over All Polarizer Angles, Before (raw) and After Calibration[a]

Config.	Filter	DoLP error				θ error		AoLP error			
		raw (%)		calib. (%)		calib. (°)		raw (°)		calib. (°)	
1	—	1.4	(0.4)	0.2	(0.6)	0.1	(0.2)	0.3	(0.8)	0.1	(0.3)
2	col. glass	4.8	(0.9)	0.3	(0.9)	0.1	(0.3)	0.4	(1.1)	0.2	(0.4)
3	hard-coated	7.8	(2.9)	0.3	(1.0)	0.1	(0.3)	0.4	(1.3)	0.1	(0.5)

[a]Values in brackets are spatial differences between image center and corners/edges as shown in Fig. 6 and discussed in the corresponding text. The DoLP error is given in percent (%). Conversions from DoLP to θ errors (in °) were calculated at the point of maximum slope at the rising flank (see text).
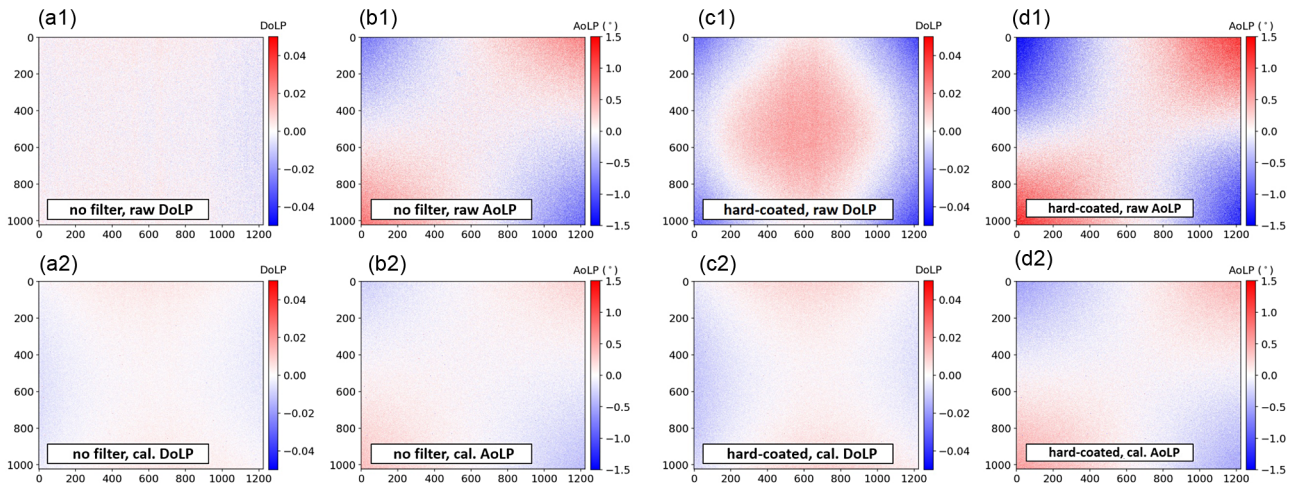
Fig. 6. DoLP (a) and (c) and AoLP (b) and (d) images for configurations 1 (no filter) and 3 (hard-coated filter). The respective mean was subtracted from each image. The upper images show raw and bottom images calibrated results. The x- and y-axes (labels not shown) refer to columns and rows of superpixels.

correspond to large errors of the angle θ used in the surface normal retrieval (Section 2.C). However, nadir geometry is not recommendable anyway because DoLP values are small then, and measurements including the Brewster angle are subject to ambiguity problems. Thus, Table 1 includes an extra column for the θ error (in units degree) when derived from (calibrated) DoLPs at the point of maximum slope ($\sim$35.9°) at the rising flank, which is considered the optimal geometry aiming at small errors.

The DoLP and AoLP reveal spatial inhomogeneities across the image sensor, shown in Fig. 6 for two examples of configuration 1 (no filter) and configuration 3 (hard-coated), both obtained for a polarizer angle $\phi = 0°$ and using f/4. The respective average has been subtracted from each subplot for better visualization of spatial patterns. In configuration 1 (columns a and b), the uncalibrated DoLP (top row) is rather homogeneous, while the AoLP shows a clear Maltese cross pattern with deviations towards the corners, which is a well-known Fresnel aberration pattern resulting from the lens being a source of polarization [36]. After calibration (bottom row), the Maltese cross pattern is still visible, but clearly reduced. In configuration 3 (columns c and d), the DoLP shows strong differences between image center and corners, most likely as a result of incidence angle on the hard-coated filter. This pattern is removed by the calibration, but another, fainter systematic pattern is produced instead with differences towards the edges. The AoLP of configuration 3 shows a stronger Maltese cross pattern than configuration 1, which is reduced by the calibration as well. To quantify spatial inhomogeneities, Table 1 includes values for the DoLP and AoLP error (in brackets), which are differences between the image center and corners in case of the AoLP and differences between center and edges in case of the DoLP (again, averages of 100×100 pixels have been used, both for the image center as well as the corners/edges).

4. MANIPULATING THE RATIO OF DoLP$_{spec}$ TO DoLP$_{water}$ BY SPECTRAL FILTERING

In the following, the measured DoLP is denoted by DoLP$_{meas}$, which is a superposition of DoLP$_{spec}$ arising from specular reflection and DoLP$_{water}$ arising from water-leaving radiance. The relative contribution of DoLP$_{spec}$ increases with θ as reflectances R_s and R_p increase (and transmittances decrease) towards the horizon [see Fig. 1(c)]. However, objects at the sea floor are better observed at smaller θ, and together with recommendations in Section 3, the point of maximum slope at the rising flank of DoLP$_{spec}$ appears to be a recommendable viewing geometry.

Apart from viewing geometry considerations, the contribution of DoLP$_{water}$ is determined by:

1. Reflection at the sea floor;
2. Backscattering inside the water.

Both sources of DoLP$_{water}$ were found to be reduced by spectral longpass filters in two different experiments. Note that the amount of backscattered light strongly depends on water constituents. The current study is limited to pure (tap) water, because the application of imaging the sea floor requires clear water.

A. Reflection at the Sea Floor and Dependence on Weather Conditions

In experiment 1, chessboard patterns were attached to the bottom of a water tank filled with 55 cm of clear tap water, which was then placed outdoors using skylight as a light source [Figs. 7(a) and 7(b)]. To investigate different ground reflectances, the used patterns had different contrasts: black and white boxes [grayscale 0 and 255, at the left in Fig. 7(a)] and black and middle-gray [grayscale 0 and 128, at the right in Fig. 7(a)].

The skylight radiance $L_{Sky}(\lambda)$ and the downwelling irradiance $E_d(\lambda)$, i.e., the integrated radiance over the full hemisphere, were measured from $\lambda = 400$ nm to $\lambda = 900$ nm using
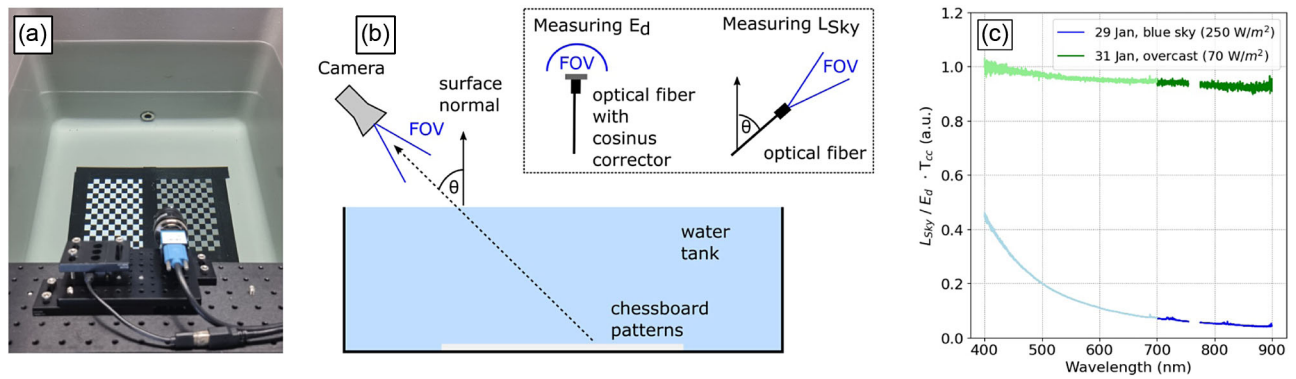
Fig. 7. (a) Photo of experiment 1. (b) Schematic of experiment 1. (c) Measured ratios of skylight radiance L_{Sky} to irradiance E_d. The y-axis is given in arbitrary units because the large acceptance angle of the cosinus corrector enabled a spectral but no radiometric measurement of its transmission T_{cc} only. In addition, NIR lines (dark colors) were scaled to connect to Vis lines (light colors).

two fiber optical spectrometers (Avantes AvaSpec-3648 and AvaSpec-ULS4096-EVO) for the visible and the near-infrared spectral range, respectively. $L_{Sky}(\lambda)$ was measured in the direction of incoming radiation producing the observed spectral reflection at the water surface using an optical fiber having a similar acceptance angle as the PFA camera's FOV [Fig. 7(b)]. The downwelling irradiance E_d was obtained by attaching a cosinus corrector (CC) to the optical fiber and pointing towards Zenith. While the relative contribution of $DoLP_{spec}$ scales with $L_{Sky}(\lambda)$, $E_d(\lambda)$ is a measure for water-leaving radiance because a fraction of the total incoming radiation eventually leaves the water again. Thus, in first approximation, the ratio $L_{Sky}(\lambda)/E_d(\lambda)$ shown in Fig. 7(c) is proportional to the ratio of used signal to interfering signal.

The experiment was repeated under two meteorological conditions, blue sky and overcast, in Bremerhaven, Germany on 29 and 31 January 2024, respectively. In both cases, the azimuthal measurement direction was to the north, with the sun being in the southeast. In overcast conditions, $L_{Sky}(\lambda)/E_d(\lambda)$ shows a rather small decrease with wavelength, which is expected as Mie scattering in clouds is only weakly wavelength-dependent (and consequently clouds are white). In contrast, for blue sky, $L_{Sky}(\lambda)/E_d(\lambda)$ shows a strong decrease with wavelength as a result of the λ^{-4} dependence of Rayleigh scattering on air molecules (leading to the blue color of the sky). At $\lambda > 850$ nm, $L_{Sky}(\lambda)/E_d(\lambda)$ is greater for overcast than blue sky. In addition, the shape of $L_{Sky}(\lambda)/E_d(\lambda)$ is more favorable in overcast conditions as being the same magnitude for $\lambda > 850$ nm (used spectral range) and $\lambda < 850$ nm (blocked range as containing $DoLP_{water}$). In contrast, for blue sky, the blocked signal ($\lambda < 850$ nm) relative to the used signal ($\lambda > 850$ nm) is much larger. Therefore, illumination under overcast conditions is beneficial for enhancing the ratio of $DoLP_{spec}$ relative to $DoLP_{water}$.

This is proven by Fig. 8, showing $DoLP_{meas}$ for blue sky (top row) and overcast (bottom row). Note, the $AoLP_{meas}$ was found to be less sensitive than $DoLP_{meas}$ and is therefore not shown. Black boxes of the chessboard pattern, having almost no ground reflectance, lead to less water-leaving radiance (although it is not zero, see experiment 2). White boxes having larger ground

reflectance produce more water-leaving radiance and thus interfere with the polarization from specular reflection, leading to artifacts. When blocking water-leaving radiance using longpass filters, artifacts get weaker. However, they remain significant under blue sky conditions while at least the black/gray pattern disappears under overcast conditions when using the 850 nm hard-coated filter. While artifacts from the black/white pattern are still present to a small degree, a white sea floor 55 cm beneath pure (tap) water represents an unrealistic extreme case so that the hard-coated filter will sufficiently avoid ground artifacts in most real-world application having overcast conditions.

In addition to the chessboard artifacts, $DoLP_{meas}$ appears skewed in the blue sky case, with smallest values in the bottom right corner. This is a result of partial polarization of the blue sky caused by Rayleigh scattering in contrast to unpolarized skylight at overcast conditions. This is another and well-known problem [20] complicating shape-from-polarization techniques under blue sky.

B. Backscattering Inside the Water

Experiment 2 investigated the remaining differences between $DoLP_{meas}$ and $DoLP_{spec}$ arising from contributions of $DoLP_{water}$ caused from backscattering within the water. The experiment (Fig. 9) required a flat and smooth water surface, and was therefore performed indoors using another 2.7 m long and 35 cm deep water tank. In this case, the tank was black and no patterns were attached to the ground so that water-leaving radiance originates predominantly from underwater scattering. A halogen lamp (unpolarized light) was used instead of skylight, for which the calibration procedure from Section 3 was repeated. The lamp illuminated a white, Lambertian screen as well as the white laboratory ceiling to resemble diffuse skylight under overcast conditions. Although this artificial illumination is different than daylight, L_{Sky}/E_d was measured and found to be comparable to the overcast scenario in experiment 1. Along a vertical line through the center of the image, $DoLP_{meas}$, was plotted as a function of the angle θ between surface normal and viewing direction, and by consecutively tilting the camera in 10° steps, angles from $\theta \approx 20°$ to $\theta \approx 80°$ could be sampled. Figures 10(a)–10(c) are the result of merging data from each tilt angle.
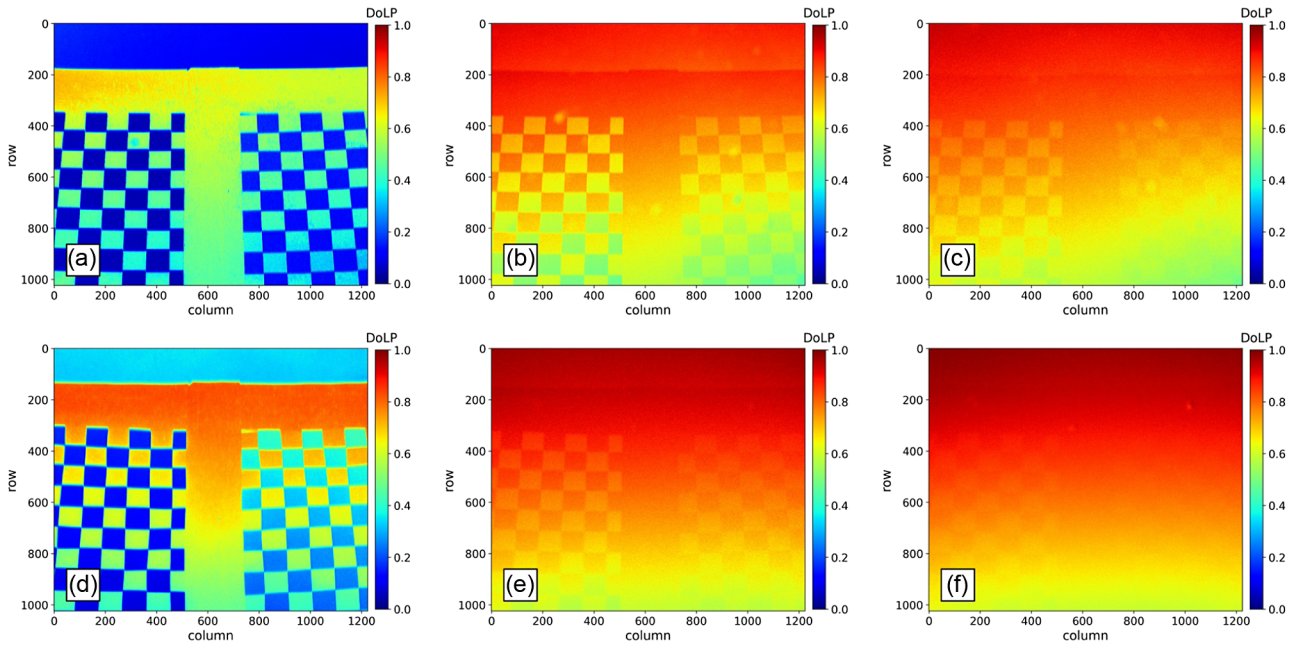
Fig. 8. Calibrated $DoLP_{meas}$ during experiment 1: (a), (b), (c) blue sky; (d), (e), (f) overcast; (a), (d) no filter; (b), (e) 850 nm colored glass; (c), (f) 850 nm hard-coated filter. The x- and y-axes refer to columns and rows of superpixels.
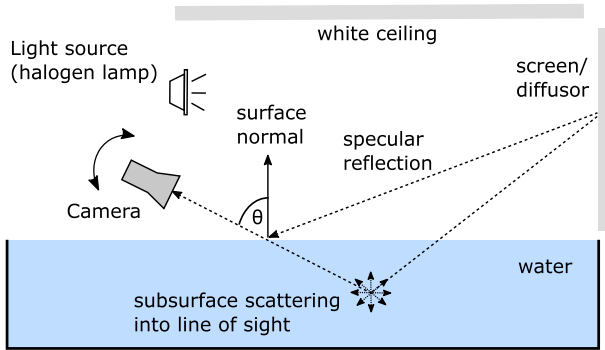
Fig. 9. Setup of experiment 2 (indoors) investigating the backscattering and the accuracy of the measured DoLP.

$DoLP_{meas}$ in Fig. 10(a) (no filter) is already close to $DoLP_{spec}$, indicating that backscattered light (plus residual light from the black bottom of the tank) only contributed a small amount to the total light reaching the PFA camera. Interestingly, $DoLP_{meas}$ matches $DoLP_{spec}$ better at large angles θ, as reflectances increase

with θ (compare Fig. 1), which indicates again the importance of strong reflections. However, differences between $DoLP_{spec}$ and $DoLP_{meas}$ are present as a result of remaining water-leaving radiance, in particular the maximum DoLP does not reach 1 and is unexpectedly found at $\theta > \theta_B$. To further investigate this, a least-squares fit ($DoLP_{Fit}$, Trust Region Reflective method as implemented in Python's *scipy* module) was performed to the measurements of $DoLP_{meas}$ according to

$$I_0 = A \cdot R_s(\theta) + B \cdot T_{s,\text{water}}(\theta)$$

$$I_{90} = A \cdot R_p(\theta) + B \cdot T_{p,\text{water}}(\theta)$$

$$DoLP_{Fit} = \left| \frac{I_0 - I_{90}}{I_0 + I_{90}} \right|. \tag{9}$$

Here, R_s and R_p are the specular reflectances from Eqs. (4) and (5), and $T_{s,\text{water}}$ and $T_{p,\text{water}}$ are corresponding transmittances for the water–air transition (see Fig. 1). A and B are weighting factors for the contributions of specular reflected and water-leaving radiances, and are obtained as fit factors. The fit (red
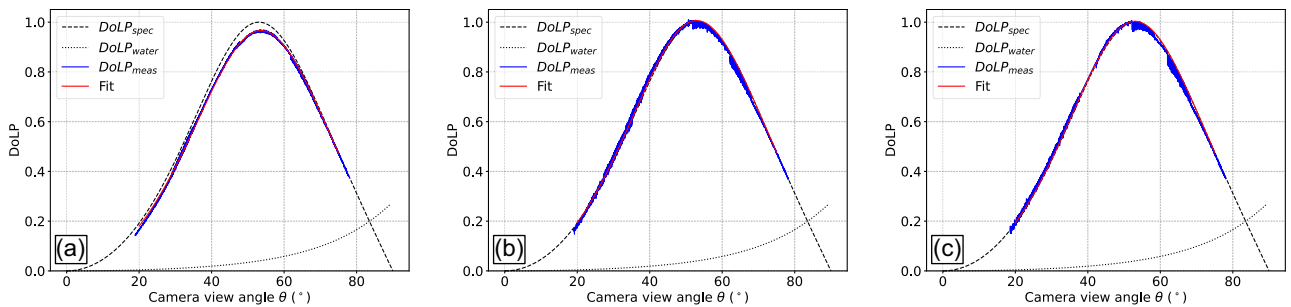
Fig. 10. Measured DoLP (calibrated) as a function of θ across a vertical line through the image sensor (see text) and fit [Eq. (9)] to the data using (a) no spectral filter, (b) 850 nm colored glass filter, and (c) 850 nm hard-coated filter. The applied f-number was f/4.

lines) is clearly able to reproduce $\text{DoLP}_{\text{meas}}$ for all cases shown in Figs. 10(a)–10(c).

Differences between $\text{DoLP}_{\text{spec}}$ and DoLP_{Fit} are reduced from ~5% in Fig. 10(a) to <1% in Figs. 10(b) and 10(c), which is comparable to levels of the calibration error, i.e., both longpass filters effectively removed the systematic influence of $\text{DoLP}_{\text{water}}$ caused by backscattering inside clear water. Increased noise is found in $\text{DoLP}_{\text{meas}}$ when longpass filters are used, resulting predominantly from the smaller illumination and thus lower signal to noise ratio. In particular, discrepancies occur in regions where individual images overlap, reflecting the increase of DoLP errors towards the image edges and corners as shown in Section 3.B.

5. RECOVERY OF WATER SURFACE NORMALS

Surface normals were recovered as outlined in Section 3.B (and described in detail in Supplement 1) using the water tank from experiment 1 in the previous section, but this time exclusively with gray-black chessboards as they produced no artifacts in $\text{DoLP}_{\text{meas}}$ when observed with the 850 nm hard-coated filter, which was used again here. A photo of the setup can be found in Fig. 2 in Section 2.C. Due to the spectral filter and an applied f-number of f/4, integration times of 500 ms were needed. Averaging over 10 images was applied to further reduce noise. The experiment was therefore again performed indoors, enabling a flat and unmoving water surface. The flat surface allowed at the same time 1) overcoming ambiguity problems of $\text{DoLP}_{\text{spec}}$ as shown below, and 2) all surface normals were known to be vertical, i.e., $w_{yz} = 0°$ and $w_{yz} = 0°$. A laboratory window opposite to the camera was opened and the specular reflection of the skylight during overcast conditions was used. Again, it was verified that the skylight was unpolarized prior

to the measurements. The PFA camera was then pitched at an angle of $\theta = 41°$ towards the water surface in order to measure close to the point of maximum slope at the rising flank of $\text{DoLP}_{\text{spec}}$. The accuracy of the adjusted camera's pitch and roll angles and therefore the error of retrieved surface normals were estimated at 0.1° using levels and an IMU.

Figures 11(a) and 11(b) show $\text{DoLP}_{\text{meas}}$ and $\text{AoLP}_{\text{meas}}$, respectively, with the trapezoidal shape being the reflection of the opened laboratory window (compare Fig. 2). Pixels outside this area of specular reflection of skylight are not useful and are excluded in the following discussion. Figure 11(c) shows the angle θ, which is retrieved by assuming $\text{DoLP}_{\text{meas}} = \text{DoLP}_{\text{spec}}(\theta)$ on the rising flank. To validate this assumption, Fig. 11(d) shows $\text{DoLP}_{\text{meas}}$ along a vertical line through the image center, averaged over pixel columns 610 to 630 (only pixel rows 0 to 1000 are plotted here because the reflection of the window does not fully reach the bottom of the image). Obviously, $\text{DoLP}_{\text{meas}}$ matches $\text{DoLP}_{\text{spec}}$ almost perfectly, i.e., the contribution of $\text{DoLP}_{\text{water}}$ is negligible, and it is entirely on the rising flank, meaning that ambiguity problems in the retrieval of θ are avoided.

Figures 11(e) and 11(f) show angles w_{yz} and w_{yx} of the retrieved surface normals in an orthogonal xyz-coordinate system (see Fig. 2). For w_{yz}, the average of the central 200×200 pixels is $-0.1° \pm 0.2°$ (the error denoting the standard deviation), which matches the expectation value of $0°$ within the adjustment uncertainty of camera pitch and roll angles. Differences increase towards the top ($0.5° \pm 0.4°$) and bottom ($-0.4° \pm 0.2°$) of the image, as well as in the corners of the reflection from the open window (e.g., $-0.8° \pm 0.9°$ in the upper right). For w_{yx}, values in the image center ($0.1° \pm 0.2°$)
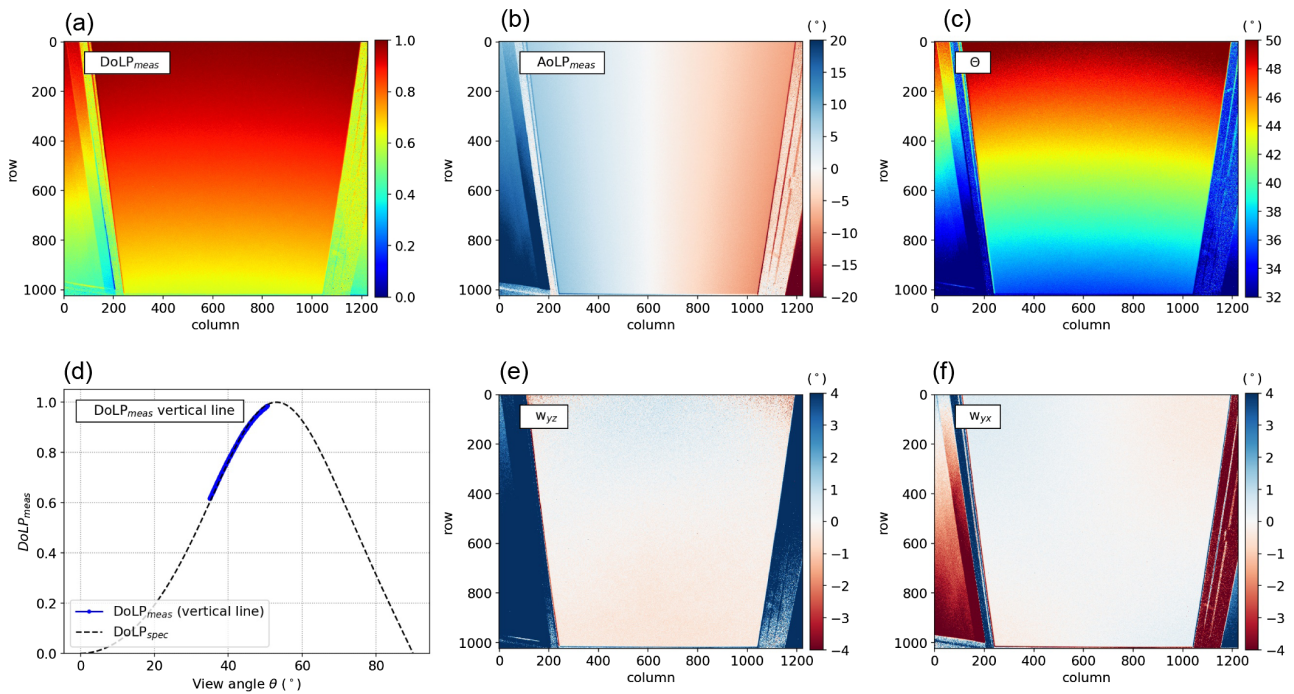
Fig. 11.   (a) $\text{DoLP}_{\text{meas}}$ and (b) $\text{AoLP}_{\text{meas}}$ using the 850 nm hard-coated filter. (c) Angles θ obtained from $\text{DoLP}_{\text{meas}}$. (d) Comparison between $\text{DoLP}_{\text{meas}}$ and $\text{DoLP}_{\text{spec}}$ along a vertical line through the image center. (e)–(f) Retrieved angles w_{yz} and w_{yx} of surface normals. The x- and y-axes refer to columns and rows of superpixels.

again meet the expected 0° and systematic differences increase towards the corners (e.g., $0.5° \pm 0.2°$ in the upper left corner).

As an explanation for these uncertainties, general features in w_{yx} are dominated mostly by the AoLP while features in w_{yz} are driven by the DoLP [24]. As a result, the Maltese cross pattern seen in the AoLP in Section 3 (Fig. 6) is reflected in w_{yx}. Increased errors of w_{yz} in the upper corners result from approaching Brewster's angle, where the $\mathrm{DoLP_{spec}}$ line's slope is small, i.e., small $\mathrm{DoLP_{meas}}$ errors result in large θ errors. In addition, geometric image distortions (e.g., barrel distortion) might be present and are not accounted for.

6. CORRECTING FOR REFRACTION AT THE SURFACE

Figure 12 shows I_{90} intensity images, which were selected because specular reflection is minimal and so the ground is seen best in I_{90}. The images have been acquired without a longpass filter in the same viewing geometry and shortly after the measurements in the previous section. Figure 12(a) is an image of the *empty* tank without water, acting as a validation for the refraction-correction. Figure 12(b) is the same, but the tank is filled with water. The water surface is ~47 cm above the chessboards, which were mounted on an elevated breadboard ~10 cm above ground.

Due to refraction at the water surface, Fig. 12(b) shows parts of the chessboards that are closer to the camera and not seen in Fig. 12(a). Vice versa, Fig. 12(a) sees more of the water tank's back wall. The chessboard boxes also appear larger (magnifying effect) in the image with water. In addition, due to the steeper light path after refraction, a gap between elevated chess boards and the drain in the background becomes apparent in the image with water.

The red box in Fig. 12(b) indicates the region for which surface normals, i.e., w_{yx} and w_{yz} were recovered in the previous section (compare Fig. 11). Only I_{90}-pixels within this region were used for the subsequent refraction-correction. First, for each pixel, the coordinates of the observed ground point are calculated in the xyz-coordinate system taking into account refraction at the surface according to Snell's law. Required inputs are the camera pitch angle, the view vector of the respective pixel, the altitude h of the camera above ground, and the water depth h_2 (the height above the water surface is $h_1 = h - h_2$) as well as angles w_{yx} and w_{yz} of the respective surface normal. Then the pixel is identified, which would see the ground coordinates if the water, and therefore refraction at the surface, was not present and the gray value of the original pixel is moved to the new pixel. Note that not all ground points seen with water occur in the image without water as explained before, and the gray value is
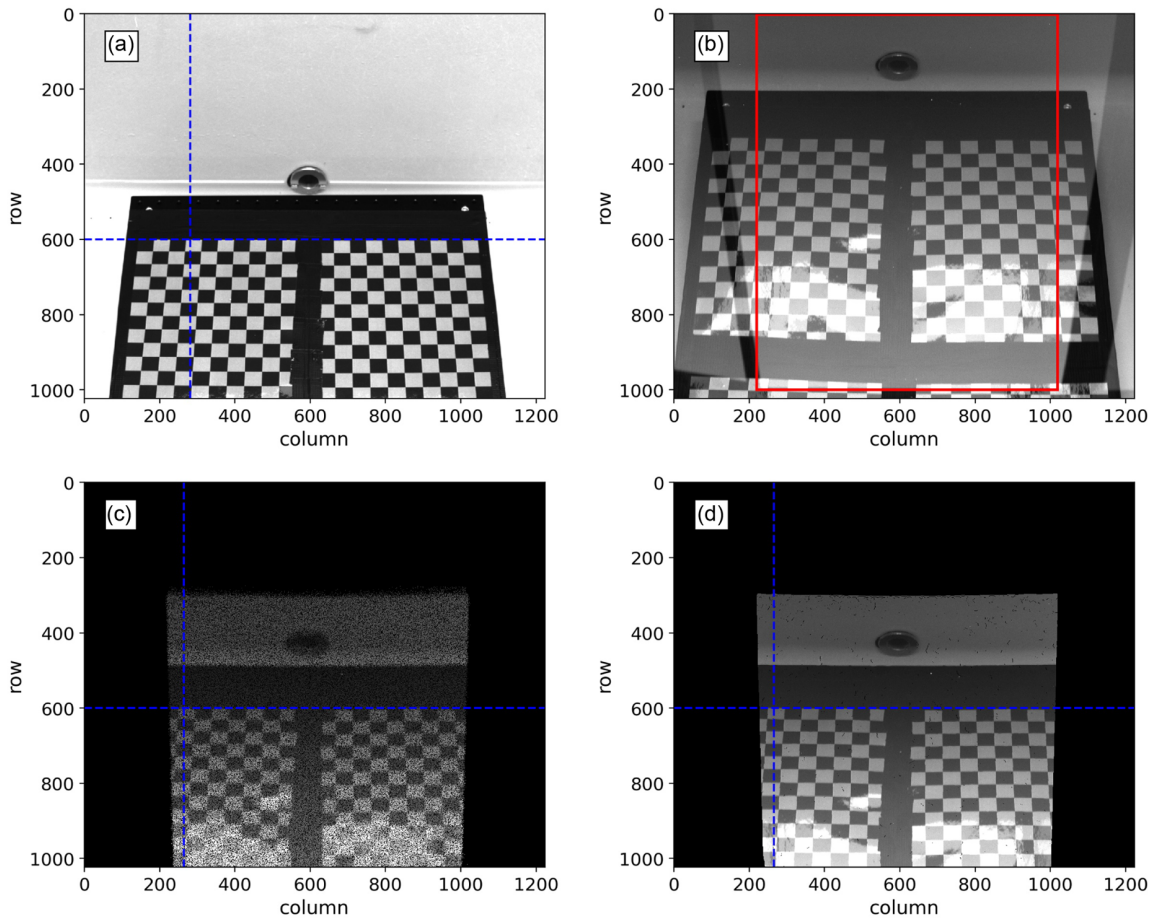
Fig. 12. I_{90} intensity images (a) without and (b) with water. The red box indicates the area in which surface normals have been retrieved (specular reflection, compare Fig. 11). (c) Refraction-corrected image of the area indicated in (b). (d) Same as (c) but smoothing w_{yx} and w_{yz} before the refraction correction. The x- and y-axes refer to columns and rows of superpixels.

rejected in that case [an example is the bottom part of the red box in Fig. 12(b)].

The resulting surface-corrected image is shown in Fig. 12(c), from which two conclusions can be drawn: 1) The chessboards are at the correct position where they appear in Fig. 12(a), meaning that w_{yx} and w_{yz} derived from polarization introduces no systematical error. 2) The corrected image looks noisy. This is a result of noise in w_{yx} and w_{yz} causing different pixels of Fig. 12(b) to be mapped to the same pixel in Fig. 12(c), while there are a lot of empty pixels in the corrected image occurring when no pixel from Fig. 12(b) is mapped to them. To reduce this noise, either the input w_{yx} and w_{yz} or the final refraction-corrected image could be smoothed. Smoothing the final image would close the gaps but at the same time reduce image sharpness. Smoothing w_{yx} and w_{yz} does not affect the sharpness of the resulting image but would cause errors in the refraction-correction procedure, at least when real small-scale patterns in w_{yx} and w_{yz} are present (e.g., as produced by waves). However, in this example, no waves were present, thus smoothing w_{yx} and w_{yz} is the better option. Fig. 12(d) is the same as Fig. 12(c) but after convolution of w_{yx} and w_{yz} with a 20×20 pixel-smoothing kernel removing almost all gaps in the corrected image.

The dashed blue lines in Figs. 12(a), 12(c), and 12(d) are used to quantify differences between the validation image and corrected images. The horizontal line indicating the upper edge of the chessboard patterns is at pixel row 600 in all images. The vertical line separating bottom chessboard boxes 6 and 7 (counted from the center) is at column 281 in Fig. 12(a) and column 265 in Figs. 12(c) and 12(d), indicating a displacement error of 16 pixels, which corresponds to 0.25° taking into account the superpixel size and the f-number of the lens used.

Note, the presented correction method is, in a strict sense, limited to flat (horizontal) obstacles on a flat sea floor. The back of the water tank with the drain is not horizontal but vertical and, as a result, the proportions of the drain in the corrected image look compressed compared to the validation image in Fig. 12(a). Nevertheless, this effect scales with the height of objects at the sea floor in relation to water depth and length of light paths, and is therefore presumably smaller for real applications, e.g., from drones.

7. CONCLUSIONS

A. Achievements

A proof of concept and accuracy estimation was presented for correction of refraction in seafloor imaging based on the recovery of water surface normals using polarization. In clear water and overcast conditions, the ratio of specular reflected radiance to water-leaving radiance was sufficiently increased by a 850 nm hard-coated longpass filter to retrieve surface normals from polarization caused by specular reflection alone. This approach is simple to implement and an alternative (in overcast conditions) to recently published more sophisticated methods [25,26], which have the advantage of being applicable to the Visible and thus overcome the drawback of large integration times required in our study. However, use of the near-infrared by applying longpass filters was a requirement here to avoid

artifacts from the ground in the measured DoLP in shallow, clear waters.

As the used PFA camera was optimized for the Visible, rigorous characterization and calibration measurements of the system were performed for different spectral longpass filters tested. Errors of the DoLP were found to strongly increase for f-numbers <f/4, especially for the hard-coated filter, which is the point at which the acceptance angle exceeds the FOV, suggesting use of larger f-numbers. However, this must be balanced against the need to keep exposure times short, avoiding motion blur when the water surface is moving. As a best practices recommendation, the f-number should be matched to the FOV, and f/4 was used throughout the present study. As another recommendation, the optimal viewing geometry is close to the point of maximum slope on the rising edge of $\text{DoLP}_{\text{spec}}(\theta)$, as this causes minimal errors of the retrieved angle θ. Calibration efforts then enable polarization uncertainties ranging from 0.1° in the image center to 0.5° in the image corners.

In an outdoor test in ~ 0.5 m deep clear water, ground artifacts from chessboard patterns were found in the measured $\text{DoLP}_{\text{meas}}$ for all investigated longpass filters under blue sky conditions (weak specular reflection). In addition, polarization of the blue skylight biased the $\text{DoLP}_{\text{meas}}$. In contrast, during overcast conditions (stronger specular reflection), ground artifacts of the gray-black patterns disappeared using the hard-coated filter, and there was no bias in $\text{DoLP}_{\text{meas}}$ as the skylight is unpolarized for that case. While the latter is well-known and was often used in previous works on surface slope retrievals, the first point is less emphasized in existing literature. We have shown that the ratio of skylight radiance (from the direction producing the observed specular reflection) to the total downwelling irradiance, L_{Sky}/E_d, is a proxy for the ratio of used signal to interfering signal and thus the presence of ground artifacts in $\text{DoLP}_{\text{meas}}$.

A more detailed analysis with a black bottom tank revealed that the contribution to $\text{DoLP}_{\text{meas}}$ from backscattering within clear water is negligible when using any of the tested longpass filters. However, backscattering at constituents in coastal waters might enhance the amount of backscattered light, which would require stronger longpass filters. This needs to be investigated in follow-up studies.

Water surface normals have been successfully retrieved from specular skylight reflection in an orthogonal world coordinate system overcoming the paraxial approximation, which is an improvement compared to most existing studies on the same topic. Systematic errors of the angle of retrieved normals with respect to Zenith were found to be in the range of experimental adjustment uncertainties of 0.1° in the image center, and increased to 0.5° (0.8°) towards the image edges (corners).

Finally, refraction in a subsurface image was removed using retrieved normals. Displacements of ground structures was as small as 10–20 pixels, corresponding to 0.25° for the optical system used. However, noise was found to be large, necessitating the use of smoothing techniques for either surface normals or the corrected intensity image to close gaps in the corrected image.

B. Limitations and Outlook

As the used commercial PFA camera was designed for the Visible, large exposure times of ∼500 ms were needed with attached longpass filters and the study therefore had to be restricted to flat and unmoving water surfaces. Nevertheless, required technical improvements appear to be realistic, e.g., the used camera has 3.45×3.45 μm large pixels. Even a similar Visible-camera with 10×10 μm large pixels would already reduce the required exposure time by a factor of 10, enabling use of the method for wavy and unstable surfaces. Improved quantum efficiency at wavelengths >850 nm would be beneficial as well. An ideal setup would use a PFA camera explicitly designed for large wavelengths in the near-infrared or SWIR (short-wave infrared) as liquid water absorption is again much stronger. Unfortunately, at the time of this study, suitable PFA cameras for the SWIR were very expensive and usually have a limited resolution. However, all findings (including equations for the surface retrieval) are applicable to improved and hopefully more affordable camera technology in the future.

The complete removal of surface refraction as demonstrated here has potential applications in the detection and localization of submerged objects from above the water, e.g., in the domains of cartography/geography, fishery, security, military, or environmental monitoring. However, many real-world applications such as improved seafloor imaging from drones would correct for distortions caused by waves and show the corrected image as if seen through a smooth water surface rather than removing the surface entirely. Due to the restriction to flat surfaces, this could not be shown here, but only minor and straightforward changes to the refraction correction in Section 6 are needed.

Disclosures. The authors declare no conflicts of interest.

Data availability. Data underlying the results presented in this paper are not publicly available at this time but may be obtained from the authors upon reasonable request.

Supplemental document. See Supplement 1 for supporting content.

REFERENCES

1. Y. Tian and S. G. Narasimhan, "Seeing through water: image restoration using model-based tracking," in *IEEE 12th International Conference on Computer Vision* (2009), pp. 2303–2310.
2. O. Oreifej, G. Shu, T. Pace, *et al.*, "A two-stage reconstruction approach for seeing through water," in *CVPR* (2011), pp. 1153–1160.
3. W. L. Weber, "Observation of underwater objects through glitter parts of the sea surface," Radiophys. Quantum Electron. **48**, 34–47 (2005).
4. I. M. Levin, V. V. Savchenko, and V. J. Osadchy, "Correction of an image distorted by a wavy water surface: laboratory experiment," Appl. Opt. **47**, 6650–6655 (2008).
5. V. Chirayath and S. A. Earle, "Drones that see through waves—preliminary results from airborne fluid lensing for centimetre-scale aquatic conservation," Aquat. Cons.: Marine Freshw. Ecosyst. **26**, 237–250 (2016).
6. V. Chirayath and A. Li, "Next-generation optical sensing technologies for exploring ocean worlds—NASA fluidcam, MiDAR, and NeMo-Net," Front. Mar. Sci. **6**, 521 (2019).
7. L. S. Dolin and D. G. Turlaev, "Polarization method for imaging through the water surface," Appl. Opt. **59**, 5772–5778 (2020).
8. L. S. Dolin, A. G. Luchinin, V. I. Titov, *et al.*, "Correcting images of underwater objects distorted by sea surface roughness," Proc. SPIE **6615**, 66150K (2007).
9. J. D. van der Laan, B. J. Redman, J. W. Segal, *et al.*, "Increased range and contrast in fog with circularly polarized imaging," Appl. Opt. **62**, 2577–2586 (2023).
10. E. Peters, M. Anders, T. Preis, *et al.*, "Performance studies of two active SWIR instrument designs for vision enhancement in indoor applications," Proc. SPIE **12737**, 127370Z (2023).
11. Y. Y. Schechner and N. Karpel, "Clear underwater vision," in *Proceedings of the 2004 IEEE Computer Society Conference on Computer Vision and Pattern Recognition (CVPR)* (2004), Vol. **1**, pp. 536–543.
12. T. W. Cronin and J. N. Marshall, "Patterns and properties of polarized light in air and water," Philos. Trans. R. Soc. B **366**, 619–626 (2011).
13. A. Nowak, J. Ernst, and F. Günther, "Inline residual stress measurement in glass production," Glass Worldwide **58**, 72–73 (2015).
14. G. Atkinson and E. Hancock, "Recovery of surface orientation from diffuse polarization," IEEE Trans. Image Process. **15**, 1653–1664 (2006).
15. G. A. Atkinson and J. D. Ernst, "High-sensitivity analysis of polarization by surface reflection," Mach. Vis. Appl. **29**, 1171–1189 (2018).
16. L. Wolff, "Diffuse reflection (intensity reflectance model)," in *Proceedings 1992 IEEE Computer Society Conference on Computer Vision and Pattern Recognition* (1992), pp. 472–478.
17. L. B. Wolff, "Diffuse-reflectance model for smooth dielectric surfaces," J. Opt. Soc. Am. A **11**, 2956–2968 (1994).
18. G. W. Kattawar and C. N. Adams, "Stokes vector calculations of the submarine light field in an atmosphere-ocean with scattering according to a Rayleigh phase matrix: effect of interface refractive index on radiance and polarization," Limnol. Oceanogr. **34**, 1453–1472 (1989).
19. L. Wolff and T. Boult, "Constraining object features using a polarization reflectance model," IEEE Trans. Pattern Anal. Mach. Intell. **13**, 635–657 (1991).
20. C. J. Zappa, M. L. Banner, H. Schultz, *et al.*, "Retrieval of short ocean wave slope using polarimetric imaging," Meas. Sci. Technol. **19**, 055503 (2008).
21. J. L. Pezzaniti, D. Chenault, M. Roche, *et al.*, "Wave slope measurement using imaging polarimetry," Proc. SPIE **7317**, 73170B (2009).
22. B. Baxter, B. A. Hooper, J. Z. Williams, *et al.*, "Polarimetric remote sensing of ocean waves," in *Oceans* (2009), pp. 1–5.
23. B. A. Hooper, B. V. Pelt, J. Z. Williams, *et al.*, "Airborne spectral polarimeter for ocean wave research," J. Atmos. Ocean. Technol. **32**, 805–815 (2015).
24. P. H. Barsic and C. R. Chinn, "Sea surface slope recovery through passive polarimetric imaging," in *Oceans* (2012), pp. 1–9.
25. M. Malinowski, A. Gilerson, E. Herrera-Estrella, *et al.*, "Polarimetric imaging of the ocean surface for the study of ocean surface roughness and wave slopes statistics," Proc. SPIE **12543**, 125430M (2023).
26. M. Malinowski, A. Gilerson, E. Herrera-Estrella, *et al.*, "Surface roughness and wave slope statistics from the multi-spectral polarimetric imaging of the ocean surface," Opt. Express **32**, 22110–22131 (2024).
27. X. Lu, J. Yang, W. Jin, *et al.*, "Polarization properties of reflected light with natural light incidence and elimination of angle of incidence ambiguity," Appl. Opt. **57**, 8549–8556 (2018).
28. M. Ottaviani, C. Merck, S. Long, *et al.*, "Time-resolved polarimetry over water waves: relating glints and surface statistics," Appl. Opt. **47**, 1638–1648 (2008).
29. M. Ottaviani, K. Stamnes, J. Koskulics, *et al.*, "Light reflection from water waves: suitable setup for a polarimetric investigation under

controlled laboratory conditions," J. Atmos. Ocean. Technol. **25**, 715–728 (2008).

30. R. Foster and A. Gilerson, "Polarized transfer functions of the ocean surface for above-surface determination of the vector submarine light field," Appl. Opt. **55**, 9476–9494 (2016).

31. A. Gilerson, C. Carrizo, A. Ibrahim, *et al.*, "Hyperspectral polarimetric imaging of the water surface and retrieval of water optical parameters from multi-angular polarimetric data," Appl. Opt. **59**, C8–C20 (2020).

32. X. Li, Z. Liu, Y. Cai, *et al.*, "Polarization 3D imaging technology: a review," Front. Phys. **11**, 1198457 (2023).

33. J. Liu, X. Lu, W. Jin, *et al.*, "Transparent surface orientation from polarization imaging using vector operation," Appl. Opt. **57**, 2306–2313 (2018).

34. J. S. Tyo, C. F. LaCasse, and B. M. Ratliff, "Total elimination of sampling errors in polarization imagery obtained with integrated microgrid polarimeters," Opt. Lett. **34**, 3187–3189 (2009).

35. J. Song, R. Abay, J. S. Tyo, *et al.*, "Transcending conventional snap-shot polarimeter performance via neuromorphically adaptive filters," Opt. Express **29**, 17758–17774 (2021).

36. R. Chipman, G. Young, and W. Lam, *Polarized Light and Optical Systems, Optical Sciences and Applications of Light* (Taylor & Francis, 2016).

37. W. Burger and M. J. Burge, *Principles of Digital Image Processing: Fundamental Techniques* (Springer, 2010).

38. G. M. Hale and M. R. Querry, "Optical constants of water in the 200-nm to 200-μm wavelength region," Appl. Opt. **12**, 555–563 (1973).

39. C. Lane, D. Rode, and T. Rösgen, "Calibration of a polarization image sensor and investigation of influencing factors," Appl. Opt. **61**, C37–C45 (2022).

40. S. B. Powell and V. Gruev, "Calibration methods for division-of-focal-plane polarimeters," Opt. Express **21**, 21039–21055 (2013).